

Article

Noble-Metal-Free $\text{Ni}_x\text{S}_y\text{-C}_3\text{N}_5$ Hybrid Nanosheet with Highly Efficient Photocatalytic Performance

Lixiao Han [†], Cong Peng [†], Jinming Huang, Linhao Sun, Shengyao Wang, Xiaohu Zhang ^{*} and Yi Yang ^{*ID}

College of Science, Huazhong Agricultural University, Wuhan 430070, China; hanlixiao@webmail.hzau.edu.cn (L.H.); pengcong@webmail.hzau.edu.cn (C.P.); huangjinming@webmail.hzau.edu.cn (J.H.); sunlinhao@mail.hzau.edu.cn (L.S.); wangshengyao@mail.hzau.edu.cn (S.W.)

^{*} Correspondence: xiaohuzhang@mail.hzau.edu.cn (X.Z.); yiyang@mail.hzau.edu.cn (Y.Y.)

[†] These authors contributed equally to this work.

Abstract: The construction of highly efficient, low-cost and noble-metal-free photocatalysts depends on photocatalytic technology. Recently, N-rich C_3N_5 has been explored as a novel carbon nitride material with a much narrower band gap (~2.2 eV) than that of traditional C_3N_4 (~2.7 eV). Planting noble-metal-free active sites on C_3N_5 to improve its photocatalytic activity is of great significance. Herein, 2D Ni_xS_y nanosheet is facially loaded on 2D C_3N_5 using a hydrothermal procedure under a low temperature. Due to the quick separation of photogenerated carries between C_3N_5 and Ni_xS_y , this inexpensive noble-metal-free $\text{Ni}_x\text{S}_y\text{-C}_3\text{N}_5$ hybrid nanosheet is highly efficient and stable as a multifunctional catalyst in various applications, including photocatalytic H_2 production from water and NO removal. Impressively, the apparent quantum yield (AQY) value for H_2 production reaches 37.0% (at 420 nm) on optimal $\text{Ni}_x\text{S}_y\text{-C}_3\text{N}_5$ hybrids, which is much higher than that of Pt- C_3N_5 material. This work opens an avenue to the fabrication of low-cost and noble-metal-free catalysts for multifunctional photocatalytic applications.



Citation: Han, L.; Peng, C.; Huang, J.; Sun, L.; Wang, S.; Zhang, X.; Yang, Y. Noble-Metal-Free $\text{Ni}_x\text{S}_y\text{-C}_3\text{N}_5$ Hybrid Nanosheet with Highly Efficient Photocatalytic Performance. *Catalysts* **2021**, *11*, 1089. <https://doi.org/10.3390/catal11091089>

Academic Editor: Juan Matos Lale

Received: 23 August 2021

Accepted: 7 September 2021

Published: 9 September 2021

Publisher's Note: MDPI stays neutral with regard to jurisdictional claims in published maps and institutional affiliations.



Copyright: © 2021 by the authors. Licensee MDPI, Basel, Switzerland. This article is an open access article distributed under the terms and conditions of the Creative Commons Attribution (CC BY) license (<https://creativecommons.org/licenses/by/4.0/>).

Keywords: $\text{Ni}_x\text{S}_y\text{-C}_3\text{N}_5$ hybrid; photocatalysis; H_2 production; NO removal; noble-metal-free catalyst

1. Introduction

Semiconductor-based photocatalytic technology is one of the most promising strategies for solving the ever-increasing energy crisis and addressing environmental pollution as well as concerns for public health [1–4]. Although numerous efforts have been made since the pioneering work on TiO_2 photoelectrodes for water splitting in 1972 [5–7], the industrialization of this technology is still unrealized due to its inefficiency and problems with implementation. In general, the photocatalytic conversion efficiency is influenced by light absorption, photogenerated carrier separation and surface reduction-oxidation reactions. Previous research has shown that the aforementioned three factors cannot be fully satisfied in one semiconductor, and the construction of hybrid materials, such as a design co-catalyst or active sites on semiconductors and semiconductor-based heterojunctions, is an effective strategy to combine the advantages of different materials to enhance photocatalytic efficiency [3,8–13]. Thus, the design of robust hybrid materials is an essential element in the photocatalytic field.

Of the various semiconductors used in photocatalytic investigation, carbon nitride has drawn enormous attention because of its low cost, metal-free status, suitable band positions, stability, environmental-friendliness, etc. [2,14–17]. Recently, a boron-doped and nitrogen-deficient strategy was reported to adjust the band positions of C_3N_4 nanosheets; Z-scheme carbon nitride-based heterostructures were fabricated with high solar-to-hydrogen efficiency (1.16% under one-sun illumination) for photocatalytic water splitting using Pt and $\text{Co}(\text{OH})_2$ as H_2 and O_2 evolving co-catalysts, respectively [18,19]. Lin et al. reported

the controlling of the reactive facets based on a carbon nitride PTI/Li⁺Cl⁻ single crystals for photocatalytic water splitting with the assistance of Pt/Co as co-catalysts [16]. In addition, C₃N₄ was decorated with oxygen-vacancy-rich BiOBr sheets to form a hybrid, which exhibited excellent photocatalytic CO₂ reduction and NO removal efficiency [20]. However, the performance of C₃N₄-based materials is seriously limited by its wide band gap (~2.7 eV). Recently, a new type of N-rich carbon nitride (C₃N₅) was synthesized using various precursors [21–26]. The structure of C₃N₅ and C₃N₄ is very similar, except that some terminal amino groups on C₃N₄ are replaced by terminal 1,2,4-triazole or 1H-1,2,3-triazole on C₃N₅ [24]. C₃N₅ could absorb visible light wavelengths longer than 600 nm and exhibited potential application in the fields of water splitting [25,26], pollutant removal [21,26], gas adsorption/sensing [25], N₂ fixing [23] and photovoltaics [22]. Recently, the photocatalytic H₂ production activity of C₃N₅ prepared from 3-amino-1,2,4-triazole was comprehensively investigated with Pt as a co-catalyst by our group [27]. However, the precious Pt is not practical for wide application. The design of low-cost noble-metal-free co-catalysts on C₃N₅ has not yet been reported in the literature. The unique visible light absorption and band position of C₃N₅ that can afford NO removal by the photocatalytic oxidation procedure, which has yet to be investigated, will be of great significance for atmosphere purification.

Herein, following the above hypothesis, 2D nickel sulfide (Ni_xS_y) is hybridized with 2D C₃N₅ to construct a noble-metal free hybrid (Ni_xS_y-C₃N₅) using a facial hydrothermal method at 120 °C. The photocatalytic H₂ production and NO oxidation properties of this hybrid are evaluated to illustrate the potential application of this material. Experimental results show that Ni_xS_y-C₃N₅ is a highly efficient, low-cost photocatalyst for H₂ production, even exceeding Pt-C₃N₅, and can produce sufficient active species participating in converting NO into harmless N-containing species such as NO₃⁻. The present work will promote the development of low-cost photocatalytic materials to address energy and environmental issues.

2. Results and Discussion

2.1. Characterization

Figure 1 depicts the X-ray diffraction (XRD) patterns of Ni_xS_y and the Ni_xS_y-C₃N₅ hybrid obtained by the facial hydrothermal method at 120 °C; Ni_xS_y-160 °C is listed for comparison. As revealed in Figure 1a, strong diffraction peaks are observed for bare Ni_xS_y material, indicating its high crystallinity, and the Ni_xS_y material prepared under hydrothermal conditions at 120 °C primarily contains NiS (PDF card of 65–3419), while some weak peaks corresponding to Ni₃S₄ (PDF card of 47–1739) can be seen. This result demonstrates that the prepared Ni_xS_y is composed of NiS and Ni₃S₄, with NiS as the main component. To obtain nickel sulfide with a single phase of NiS or Ni₃S₄, the hydrothermal temperature for nickel sulfide preparation is adjusted and is shown in Figure 1a and Figure S1. As can be seen, the nickel sulfides obtained under temperatures from 100 to 170 °C are mixed phases of NiS and Ni₃S₄, with the main phase changing from NiS to Ni₃S₄. Taking Ni_xS_y at 160 °C (Ni_xS_y – 160 °C) as an example (Figure 1a), it is mainly composed of Ni₃S₄ but some small peaks corresponding to NiS can also be found. It should be noted that a new phase of NiS₂ in Ni₃S₄ is observed when the hydrothermal temperature is increased to 200 °C. The above result reveals that it is difficult to prepare nickel sulfide with a single phase using this facial method. Notably, it has been reported that nickel sulfides have multiple crystalline phases (i.e., NiS, Ni₃S₄, Ni₃S₂, NiS₂, Ni₇S₆, and Ni₉S₈) depending on the relative concentration of nickel and sulfur precursors in the synthetic system, and the mixed phase of these nickel sulfides have exhibited better performance [28–30]. Thus, the materials containing Ni_xS_y mentioned in the following sections are all synthesized under 120 °C unless otherwise specified.

As displayed in Figure 1b, two distinct peaks corresponding to (100) and (002) planes of C₃N₅ are observed, which is in agreement with our previous work and the related literature [23,25,27]. For the hybrid of Ni_xS_y-C₃N₅, the two peaks for C₃N₅ exhibit no obvious shift, indicating that the present hydrothermal procedure does not destroy the

basic structure of C_3N_5 . Briefly, no obvious peaks corresponding to Ni_xS_y are found for 1.0 wt% $Ni_xS_y-C_3N_5$, which is likely due to the low loading amount of Ni_xS_y . However, some weak peaks attributed to Ni_xS_y are observed when the loading amount of Ni_xS_y is increased to 3.0 wt%, indicating the successful fabrication of the $Ni_xS_y-C_3N_5$ hybrid.

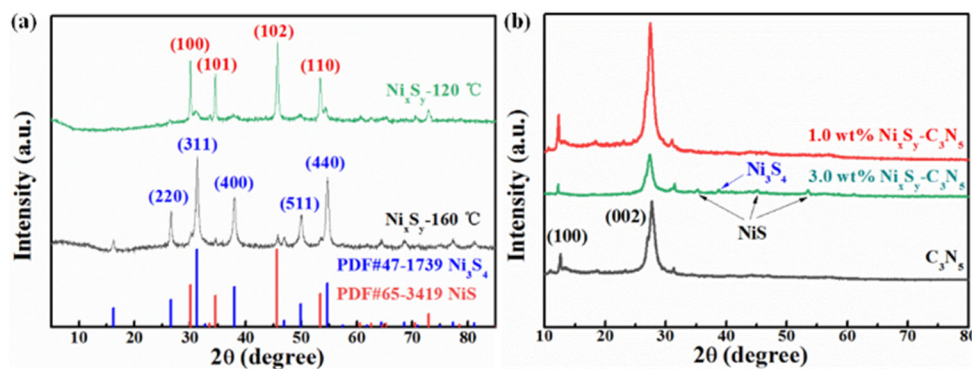


Figure 1. XRD patterns of (a) Ni_xS_y prepared using a hydrothermal procedure at 120 and 160 °C, and (b) C_3N_5 and $Ni_xS_y-C_3N_5$ with different Ni_xS_y loading amounts prepared using a hydrothermal procedure at 120 °C.

Generally, C_3N_5 exhibits the micro morphology of 2D nanosheet according to our previous work. Figure 2 displays the TEM images of Ni_xS_y and $Ni_xS_y-C_3N_5$ hybrids. In brief, Ni_xS_y exhibits irregular 2D nanosheets (Figure 2a), which is similar to that of C_3N_5 . HRTEM images of Ni_xS_y (Figure 2b) confirm the fact that it is composed of NiS and Ni_3S_4 , and clear lattice fringes of 0.25 and 0.28 nm corresponding to NiS (101) and Ni_3S_4 (311), respectively, are observed. This result is in good agreement with the above-mentioned XRD analysis. As depicted in Figure 2c for 1.0 wt% $Ni_xS_y-C_3N_5$, the sheets of Ni_xS_y and C_3N_5 contact tightly with each other, indicating that the $Ni_xS_y-C_3N_5$ is a 2D/2D nanosheet hybrid and the hydrothermal procedure for Ni_xS_y preparation has no obvious influence on the structure of C_3N_5 . C_3N_5 possesses an amorphous structure as shown in our previous work. The HRTEM image of 1.0 wt% $Ni_xS_y-C_3N_5$ (Figure 2d) conveys that amorphous C_3N_5 is combined with Ni_xS_y , for which clear lattice fringes of 0.25 and 0.28 nm corresponding to NiS (101) and Ni_3S_4 (311), respectively, are also be observed. The TEM results confirm the successful fabrication of the $Ni_xS_y-C_3N_5$ hybrid.

To further investigate the components of the hybrid, we performed scanning electron microscope (SEM) and Energy-dispersive X-ray spectroscopy (EDS) element mapping of 1.0 wt% $Ni_xS_y-C_3N_5$, as shown in Figure 3. As seen in the figure, $Ni_xS_y-C_3N_5$ exhibits the basic morphology of nanosheets, which is in good agreement with the results of TEM. In addition, the hybrid is composed mainly of C, N, Ni and S elements, and each element disperses uniformly in the observed region from the mapping images. The high dispersion of Ni_xS_y on C_3N_5 will be favorable for subsequent photocatalytic performance.

Figure 4 and Figure S2 show the XPS spectra of $Ni_xS_y-C_3N_5$ to determine the state of each element in the hybrid. As exhibited in the survey spectrum of Figure S2a, C, N, Ni and S are all observed in 1.0 wt% $Ni_xS_y-C_3N_5$, indicating the successful fabrication of the hybrid, which is in good agreement with the above results of XRD, TEM and SEM analyses. The regional spectra of C 1s and N 1s (Figure S2b,c) are similar to that of C_3N_5 in our previous work [27], and no obvious shift is observed for the corresponding peak position, revealing that the hydrothermal procedure for the $Ni_xS_y-C_3N_5$ preparation has no obvious influence on the structure of C_3N_5 . The high-resolution XPS spectrum of S 2p is shown in Figure 4a, in which the peak at ~168 eV represents the residual sulfate group originating from the hydrothermal procedure. Two peaks at ~162.3 and ~163.1 eV corresponding to S 2p_{3/2} and S 2p_{1/2}, respectively, are observed, demonstrating the existence of a metal-sulfur (Ni-S) bond and sulfur ion [30–32]. Two distinct spin-orbit peaks at ~855 (Ni 2p_{3/2}) and 873 eV (Ni 2p_{1/2}), along with two satellite peaks (identified as “Sat.”), are observed in the

high-resolution XPS spectrum of Ni 2p (Figure 4b), suggesting the existence of nickel ions in the $\text{Ni}_x\text{S}_y\text{-C}_3\text{N}_5$ hybrid [30,31,33]. These results further confirm that the $\text{Ni}_x\text{S}_y\text{-C}_3\text{N}_5$ hybrid was successfully constructed.

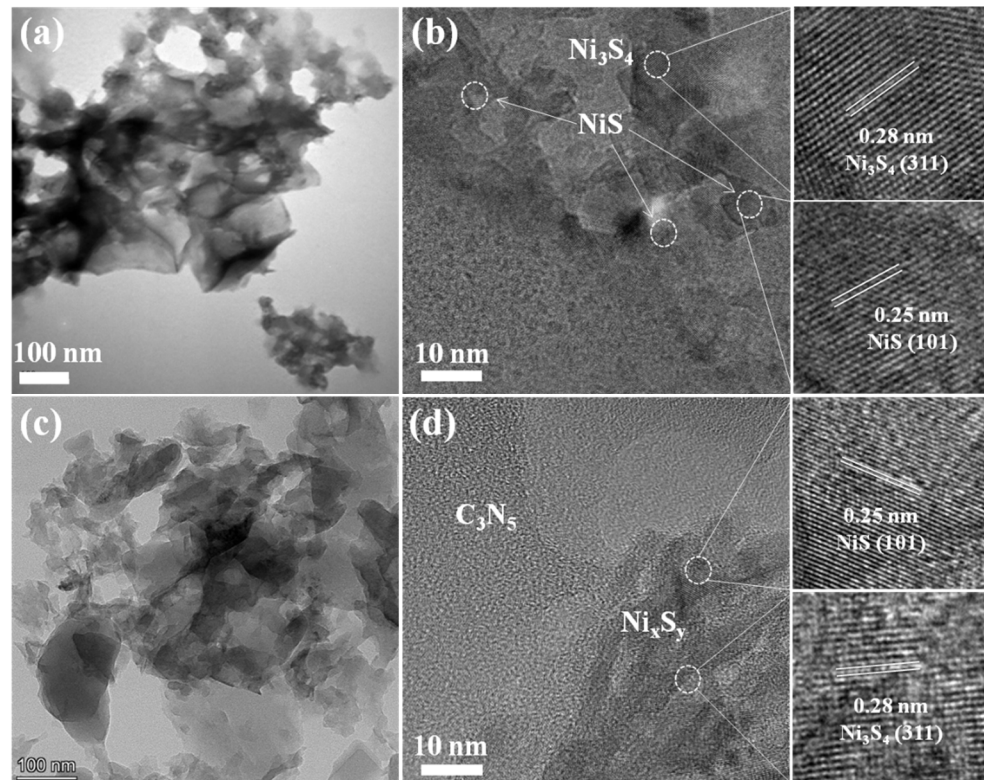


Figure 2. TEM and HRTEM images of Ni_xS_y (a,b) and 1.0 wt% $\text{Ni}_x\text{S}_y\text{-C}_3\text{N}_5$ (c,d).

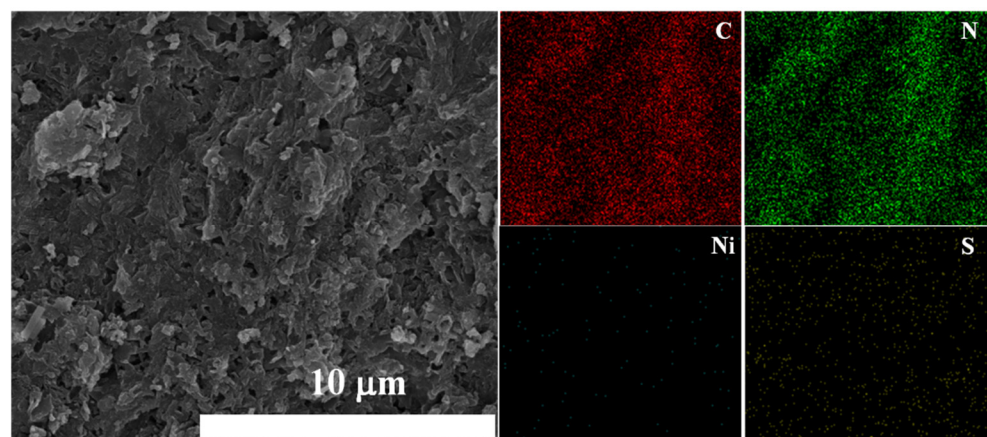


Figure 3. SEM and element mapping images of 1.0 wt% $\text{Ni}_x\text{S}_y\text{-C}_3\text{N}_5$.

The DRS spectra of Ni_xS_y , C_3N_5 and $\text{Ni}_x\text{S}_y\text{-C}_3\text{N}_5$ were recorded to provide a direct comparison of their light absorption properties, which play an important role in photocatalytic performance. As revealed in Figure 5, C_3N_5 exhibits strong absorption in the visible light wavelength longer than 600 nm due to its narrow band gap (~ 2.25 eV), as shown in our previous work [27]. Ni_xS_y can absorb the whole visible light region due to its black color. In addition, the visible light absorption property of $\text{Ni}_x\text{S}_y\text{-C}_3\text{N}_5$ displays the combination of the two components, demonstrating the successful construction of the $\text{Ni}_x\text{S}_y\text{-C}_3\text{N}_5$ hybrid. The excellent visible-light-responsive ability of $\text{Ni}_x\text{S}_y\text{-C}_3\text{N}_5$ is favorable for photocatalytic applications.

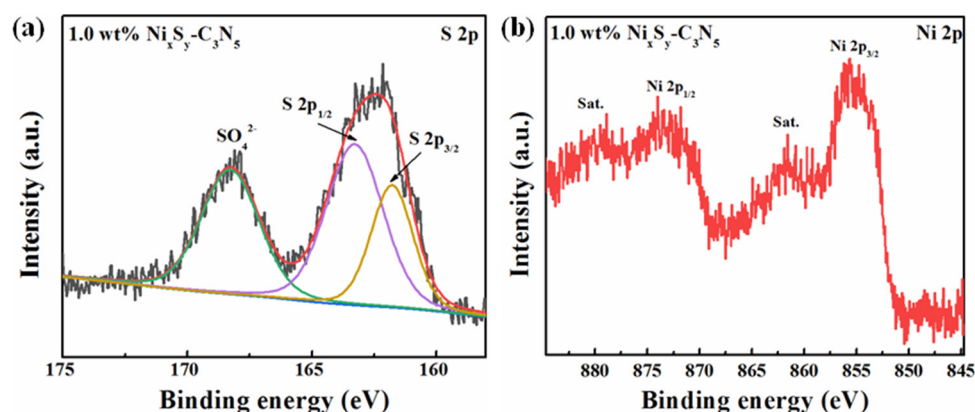


Figure 4. High-resolution XPS spectrum of S 2p (a) and Ni 2p (b).

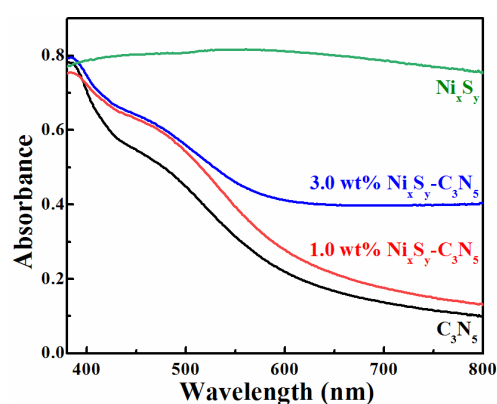


Figure 5. DRS spectra of Ni_xS_y , C_3N_5 and $\text{Ni}_x\text{S}_y\text{-C}_3\text{N}_5$.

2.2. Photocatalytic H_2 Production Performance

The photocatalytic activity of $\text{Ni}_x\text{S}_y\text{-C}_3\text{N}_5$ was first evaluated for H_2 production under visible light irradiation ($\lambda > 420 \text{ nm}$), with TEOA as the sacrificial reagent. Our previous work demonstrated that no obvious H_2 production was observed on pristine C_3N_5 due to the lack of co-catalyst [27]. In addition, the control experiment displayed that H_2 production is extremely limited on pristine Ni_xS_y . As depicted in Figure 6a, the H_2 production rate can be greatly elevated when 0.5 wt% Ni_xS_y is loaded on C_3N_5 , demonstrating that Ni_xS_y can facilitate the separation of photogenerated carriers of C_3N_5 and serve as an active site for H_2 production. This result is in good agreement with the literature, where nickel sulfide is widely taken as a catalyst for photo- or electro-catalytic water reduction [31–35]. The influence of Ni_xS_y loading amounts on the H_2 production rate of $\text{Ni}_x\text{S}_y\text{-C}_3\text{N}_5$ was also investigated and is shown in Figure 6a. The H_2 production rate increases when increasing the loading amount of Ni_xS_y , and a platform is obtained when the fraction of Ni_xS_y changes from 1.0 wt% to 3.0 wt%. However, a decrease in photoactivity is observed for 4.0 wt% $\text{Ni}_x\text{S}_y\text{-C}_3\text{N}_5$, which may be related to the influence of excessive Ni_xS_y on the visible light absorption of C_3N_5 . Generally, the initial amount of the S source should be higher than that of the Ni source in the nickel sulfide preparation process. Thus, taking 3.0 wt% $\text{Ni}_x\text{S}_y\text{-C}_3\text{N}_5$ as an example, the influence of the initial mol ratio of Ni/S ($\text{Ni}(\text{NO}_3)_2/\text{TAA}$) on the H_2 production rate was investigated and is shown in Figure S3; the optimal Ni/S reaction condition is confirmed as 1/3, and the highest H_2 production rate is $\sim 1595 \mu\text{mol/h}$.

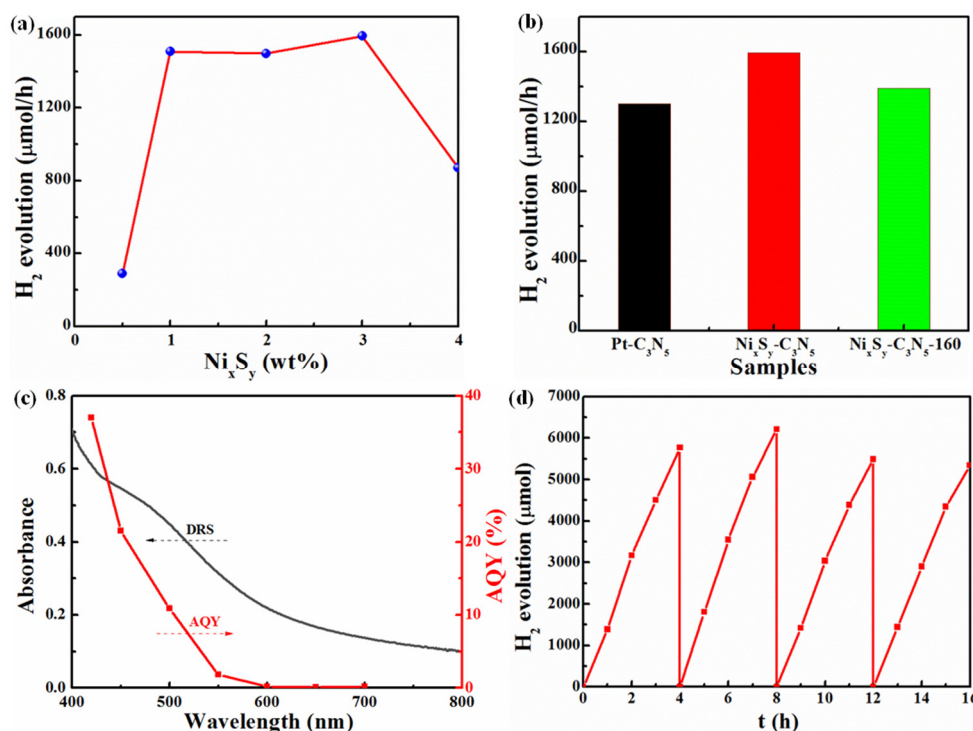


Figure 6. (a) Influence of Ni_xS_y loading amount on the H₂ production rate of Ni_xS_y-C₃N₅ hybrid. (b) Comparison of H₂ production rate over Pt-C₃N₅, Ni_xS_y-C₃N₅ and Ni_xS_y-C₃N₅-160. (c) Change tendency of AQY values along with irradiated wavelength on Ni_xS_y-C₃N₅. (d) Long-term test for H₂ production on Ni_xS_y-C₃N₅. Conditions: 45 mg catalyst, 30 mL 10 vol% TEOA/H₂O aqueous solution, λ > 420 nm (for a,b,d), λ = 420, 450, 500, 550, 600, 650, 700 nm (for c).

As mentioned above, the main phase of Ni_xS_y is NiS, while a slight amount of Ni₃S₄ also exists in the catalyst. To explore the main phase of nickel sulfide, which plays a dominant role in photocatalytic H₂ production activity, taking 3.0 wt% Ni_xS_y-C₃N₅ as a reference, the sample of 3.0 wt% Ni_xS_y-C₃N₅-160 (prepared at 160 °C hydrothermal treatment, with the main component of Ni_xS_y being Ni₃S₄; see Figure 1a) was also tested for H₂ production under the same photocatalytic condition. As shown in Figure 6b, the difference in H₂ production rates between 3.0 wt% Ni_xS_y-C₃N₅ and 3.0 wt% Ni_xS_y-C₃N₅-160 is slight, demonstrating that both NiS and Ni₃S₄ in Ni_xS_y can act as electron traps and active sites to greatly enhance the photocatalytic activity for H₂ production. To evaluate the efficiency of the Ni_xS_y co-catalyst, Pt nanoparticle, a widely used co-catalyst in photocatalysis, was taken as reference. As shown in Figure 6b, the H₂ production rate of 3.0 wt% Ni_xS_y-C₃N₅ is higher than that of 1.0 wt% Pt-C₃N₅ (the optimal Pt loaded amount is 1.0 wt% according to our previous work [27]), NiS [33,34] and NiS/C₃N₄ [36,37] materials (see Table 1). This result conveys that the present Ni_xS_y may be a competitive alternative to noble metals such as Pt as a co-catalyst utilized in photocatalytic H₂ production.

Table 1. The comparison of the photocatalytic H₂ production performance of the Ni_xS_y-C₃N₅ with some reported catalysts.

Photocatalysts	Reaction Conditions	H ₂ Production Rate μmol g ⁻¹ h ⁻¹	Ref.
Pt/C ₃ N ₅	300 W Xe lamp (λ > 420 nm), TEOA	28,956	[27]
NiS/ZnIn ₂ S ₄	320 W Xe lamp (λ > 420 nm), Lactic Acid	3333	[33]
NiS/CQDs/ZnIn ₂ S ₄	300 W Xe lamp (λ > 420 nm), TEOA	568	[34]
g-C ₃ N ₄ /1.5% NiS	300 W Xe lamp (λ > 420 nm), TEOA	395	[36]
NiS/g-C ₃ N ₄	300 W Xe lamp (λ > 420 nm), TEOA	16,400	[37]
Ni _x S _y -C ₃ N ₅	300 W Xe lamp (λ > 420 nm), TEOA	35,444	this work

Taking 3.0 wt% $\text{Ni}_x\text{S}_y\text{-C}_3\text{N}_5$ as a model, the change tendency of AQY values along with the irradiated wavelength is shown in Figure 6c; the AQY values decrease gradually when the monochromatic light changes from 420 to 700 nm. This result demonstrates that the photocatalytic H_2 production of $\text{Ni}_x\text{S}_y\text{-C}_3\text{N}_5$ is dominated by its visible light absorption property. The highest AQY value is 37.0% at 420 nm light irradiation, which is higher than that of $\text{Pt-C}_3\text{N}_5$ exhibited in our previous work [27]. In addition, the $\text{Ni}_x\text{S}_y\text{-C}_3\text{N}_5$ hybrid can also work under 700 nm monochromatic light irradiation with an AQY value of 0.2%. To evaluate the cyclicity and durability of the present hybrid material for H_2 production, a long-term test under visible light irradiation was conducted on 3.0 wt% $\text{Ni}_x\text{S}_y\text{-C}_3\text{N}_5$. As revealed in Figure 6d, the hybrid exhibits excellent stability for H_2 production in the four test runs during a total of 16 h of visible light irradiation. The stability of $\text{Ni}_x\text{S}_y\text{-C}_3\text{N}_5$ is also confirmed by the XRD and DRS curves of the photocatalytic H_2 production test, as depicted in Figure 7. No obvious change in the peak number and position is observed for $\text{Ni}_x\text{S}_y\text{-C}_3\text{N}_5$ before and after the photocatalytic test. In addition, there is only a slight change in the visible light responsive property of $\text{Ni}_x\text{S}_y\text{-C}_3\text{N}_5$ after the photocatalytic test when compared with the pristine material. The nickel concentration in the solution after the photocatalytic reaction was determined to be 20.3 ppb by ICP-MS. Thus, the leaching rate of Ni was 0.14%, which is negligible. These results further confirm the structural stability of $\text{Ni}_x\text{S}_y\text{-C}_3\text{N}_5$ during the photocatalysis procedure.

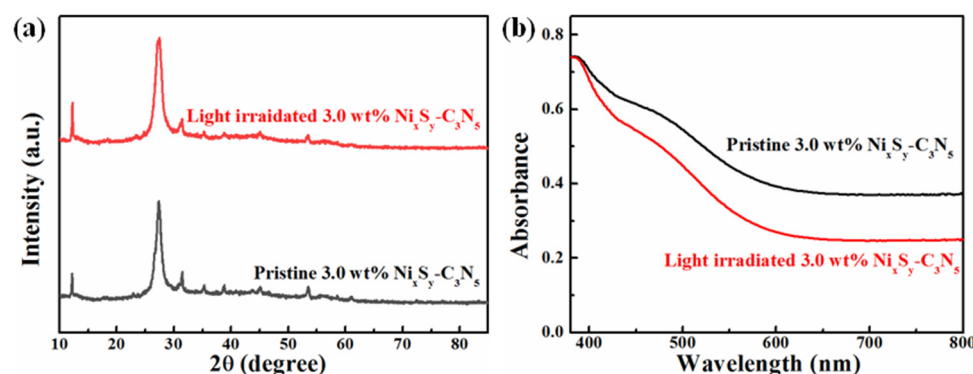


Figure 7. Comparison of (a) XRD and (b) DRS curves of pristine and light irradiated $\text{Ni}_x\text{S}_y\text{-C}_3\text{N}_5$.

2.3. Photocatalytic NO Oxidation Performance

Figure 8a depicts the photocatalytic NO oxidation performance of $\text{Ni}_x\text{S}_y\text{-C}_3\text{N}_5$ and C_3N_5 ; quick removal of NO is observed, and the removal ratio reaches equilibrium during a short (~20 min) test in the continuous flow reaction system. The control experiment shows that no obvious activity for NO removal is observed on the pristine Ni_xS_y . The NO removal efficiency on pristine C_3N_5 is ~35%, which can be attributed to its wide light absorption property and suitable band position for O_2 molecular activation and the generation of reactive oxygen species (ROS, such as $\bullet\text{OH}$, $\bullet\text{O}_2^-$ and $^1\text{O}_2$), which participate in the subsequent photocatalytic NO oxidation. Generally, the production of $\bullet\text{O}_2^-$ and $^1\text{O}_2$ follows the equations of $\text{O}_2 + e^- \rightarrow \bullet\text{O}_2^-$ and $\bullet\text{O}_2^- + h^+ \rightarrow ^1\text{O}_2$ [11,38]. In addition, the production $\bullet\text{OH}$ follows the procedure of $\bullet\text{O}_2^- + 2\text{H}^+ \rightarrow \text{H}_2\text{O}_2 \rightarrow \bullet\text{OH}$, since the VB position of C_3N_5 is more negative than the potential of $\bullet\text{OH}/\text{H}_2\text{O}$ (2.38 V vs. NHE, pH = 0) according to our previous work [11,27]. The corresponding NO removal value can be improved to ~40% when 0.5 and 1.0 wt% Ni_xS_y are loaded on C_3N_5 , which is much higher than that of the C_3N_4 materials (see Table 2) [39–41]. However, a decrease in NO removal efficiency is observed with a higher loading amount of Ni_xS_y (such as 3.0 wt%). It should be noted that excessive Ni_xS_y may cover the surface of C_3N_5 and then influence the light absorption by C_3N_5 . The improved photocatalytic performance is related to the electron transfer between C_3N_5 and Ni_xS_y , as well as the enhanced efficiency for ROS generation, as will be discussed in the following section. The durability of 1.0 wt% $\text{Ni}_x\text{S}_y\text{-C}_3\text{N}_5$ on photocatalytic NO removal was tested under 2 h of light irradiation, as shown in Figure 8b;

the removal ratio is maintained in the long-term test, revealing the excellent photocatalytic stability of $\text{Ni}_x\text{S}_y\text{-C}_3\text{N}_5$. The cycling performance of 1.0 wt% $\text{Ni}_x\text{S}_y\text{-C}_3\text{N}_5$ on photocatalytic NO removal is depicted in Figure 8c; there is only a slight decrease after six test runs, demonstrating the excellent photocatalytic repeatability of the present hybrid. Generally, the products of photocatalytic NO oxidation are considered to be NO_2 and NO_3^- . The production of NO_2 is directly recorded on the NO_x analyzer shown in Figure 8d. For NO_3^- detection, the irradiated $\text{Ni}_x\text{S}_y\text{-C}_3\text{N}_5$ samples are re-dispersed in water and then filtered. Finally, the transparent filtrate is analyzed by ion chromatography with NaNO_3 as a reference. As displayed in Figure 8e, the production of NO_3^- during NO removal is confirmed qualitatively. Notably, the selectivity for NO_3^- production is estimated to be ~70%, based on NO removal efficiency and residual NO_2 amount (Figure 8a,d).

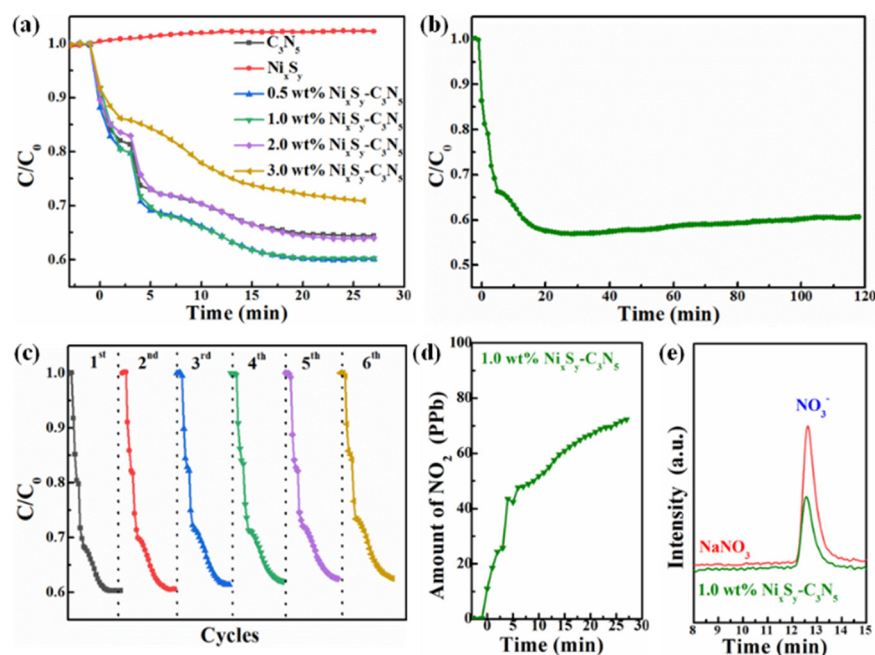


Figure 8. (a) Comparison of photocatalytic NO removal behaviors on Ni_xS_y , C_3N_5 and $\text{Ni}_x\text{S}_y\text{-C}_3\text{N}_5$. Durability (b) and cyclability (c) of photocatalytic NO removal on 1.0 wt% $\text{Ni}_x\text{S}_y\text{-C}_3\text{N}_5$. Detection of NO_2 (d) and NO_3^- (e) during photocatalytic NO removal on $\text{Ni}_x\text{S}_y\text{-C}_3\text{N}_5$.

Table 2. The comparison of the photocatalytic NO removal performance of the $\text{Ni}_x\text{S}_y\text{-C}_3\text{N}_5$ with some reported catalysts.

Photocatalysts	Reaction Conditions	NO Removal Efficiency (%)	Ref.
Mo-g- C_3N_4 /g- C_3N_4	flow reactor, metal halide lamp, >420 nm	36.0	[39]
g- C_3N_4 / $\text{BO}_{0.2}\text{N}_{0.8}$	flow reactor, metal halide lamp, >420 nm	30.2	[40]
N-Vacancies g- C_3N_4	flow reactor, Xe lamp, >420 nm	32.8	[41]
$\text{Ni}_x\text{S}_y\text{-C}_3\text{N}_5$	flow reactor, visible LED	40.0	this work

Generally, photogenerated h^+ and the series of ROS play significant roles in the photocatalytic NO oxidation procedure. To explore active species that participate in the reaction of NO removal, a series of trapping agent experiments were conducted, in which $\text{Na}_2\text{C}_2\text{O}_4$, tert-butanol (TBA), p-benzoquinone (PBQ) and β -carotene were used as scavengers for h^+ , $\bullet\text{OH}$, $\bullet\text{O}_2^-$ and $^1\text{O}_2$, respectively [42]. As can be seen in Figure 9a, the photocatalytic NO removal efficiency is inhibited to different extents when different trapping agents are added, demonstrating that all of the above-mentioned species can participate in the procedure for NO removal. In addition, the dominant species are $\bullet\text{O}_2^-$ and $^1\text{O}_2$, since the NO removal efficiency is greatly inhibited when the two species are captured. Electron spin resonance (ESR) spectra were recorded to monitor the formation of

the main active species of $\bullet\text{O}_2^-$ and $^1\text{O}_2$. As revealed in Figure 9b,c, characteristic signals for DMPO- $\bullet\text{O}_2^-$ and TEMPO (product of TEMP oxidized by $^1\text{O}_2$) were detected [42–44], and the signal intensity for $\text{Ni}_x\text{S}_y\text{-C}_3\text{N}_5$ was higher than that of pristine C_3N_5 under light irradiation, demonstrating that greater amounts of ROS can be generated on the $\text{Ni}_x\text{S}_y\text{-C}_3\text{N}_5$ hybrid. The result of the EPR analysis is in good agreement with the results of the photocatalytic performance.

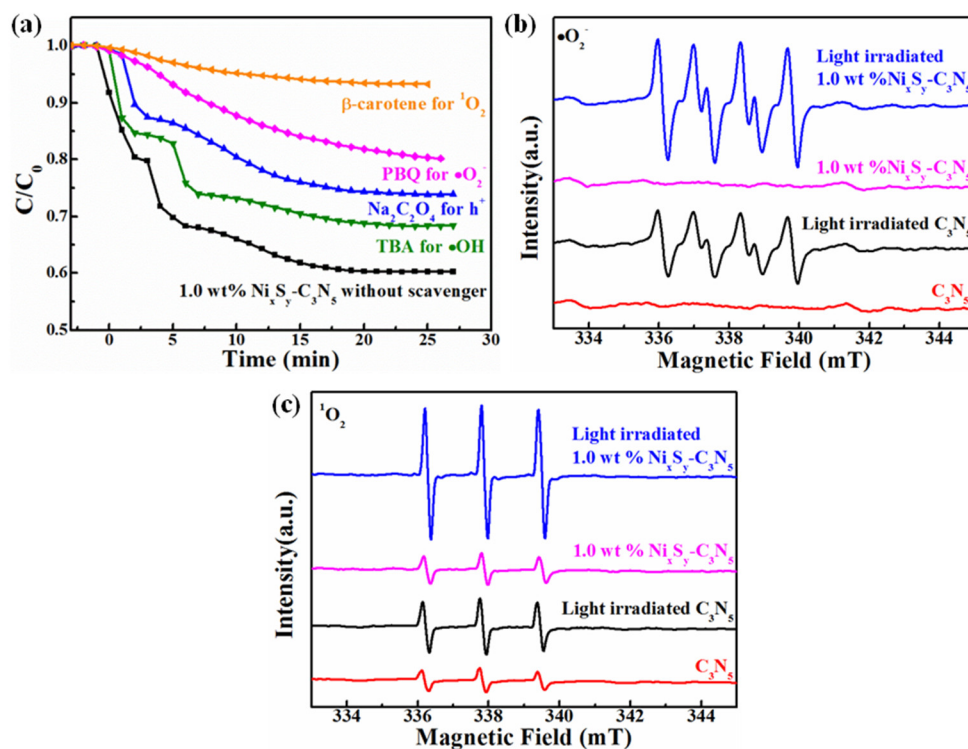


Figure 9. (a) Trapping agent experiments for photocatalytic NO removal. ESR spectra of DMPO- $\bullet\text{O}_2^-$ (b) and TEMPO (c) for ROS detection.

BET analysis was first conducted to explore the factors affecting the high photocatalytic performance of $\text{Ni}_x\text{S}_y\text{-C}_3\text{N}_5$ compared with C_3N_5 . As shown in Figure S4, the specific surface area of $\text{Ni}_x\text{S}_y\text{-C}_3\text{N}_5$ ($10.32\text{ m}^2/\text{g}$) is almost equal to that of C_3N_5 ($10.60\text{ m}^2/\text{g}$), showing that this factor cannot afford the enhanced photoactivity for $\text{Ni}_x\text{S}_y\text{-C}_3\text{N}_5$. Considering that nickel sulfide is often taken as an active site for H_2 production in the field of photo- and electro-catalysis, the influence of Ni_xS_y on the separation of e^-/h^+ pairs generated from C_3N_5 under light excitation was investigated using steady-state and time-resolved PL as well as photocurrent-time and EIS behaviors. As depicted in Figure 10a, the PL intensity of C_3N_5 is dramatically quenched by Ni_xS_y , demonstrating that the loading of Ni_xS_y can significantly restrain the e^-/h^+ recombination of C_3N_5 under light excitation and Ni_xS_y can serve as electron traps to facilitate the photogenerated electron transfer from C_3N_5 to Ni_xS_y [15,45]. This viewpoint is further supported by the time-resolved fluorescence spectra (TRFS) shown in Figure 10b; the PL decay rate on $\text{Ni}_x\text{S}_y\text{-C}_3\text{N}_5$ is slower than that of pristine C_3N_5 , and the fluorescence lifetime of $\text{Ni}_x\text{S}_y\text{-C}_3\text{N}_5$ (11.56 ns) is longer than that of pristine C_3N_5 (8.50 ns), demonstrating that the recombination of photogenerated e^-/h^+ pairs on C_3N_5 is restrained by Ni_xS_y through efficient internal electron transfer [15,46]. The generation and separation of e^-/h^+ pairs on $\text{Ni}_x\text{S}_y\text{-C}_3\text{N}_5$ and C_3N_5 is also reflected in their photocurrent-time behaviors. Figure 10c shows the change tendency of photocurrent curves of the two materials along with commutative light-on and light-off operation. The high current value was recorded when the work electrode was irradiated by the Xe-lamp, and the value vanished suddenly when the light was turned down, indicating that the current is generated after the material is excited. In addition, the generation of photocurrent

is repeatable. Moreover, the photocurrent value recorded on $\text{Ni}_x\text{S}_y\text{-C}_3\text{N}_5$ is much higher than that of C_3N_5 , demonstrating that the separation of e^-/h^+ pairs in $\text{Ni}_x\text{S}_y\text{-C}_3\text{N}_5$ under light irradiation is greatly improved. This result is in accordance with the conclusions of the PL analysis. A smaller radius was obtained on $\text{Ni}_x\text{S}_y\text{-C}_3\text{N}_5$ from the EIS Nyquist plots, as shown in Figure 10d, revealing the lower charge transfer resistance of $\text{Ni}_x\text{S}_y\text{-C}_3\text{N}_5$ [15,47]. The above results convey that $\text{Ni}_x\text{S}_y\text{-C}_3\text{N}_5$ possesses quicker internal charge migration than bare C_3N_5 .

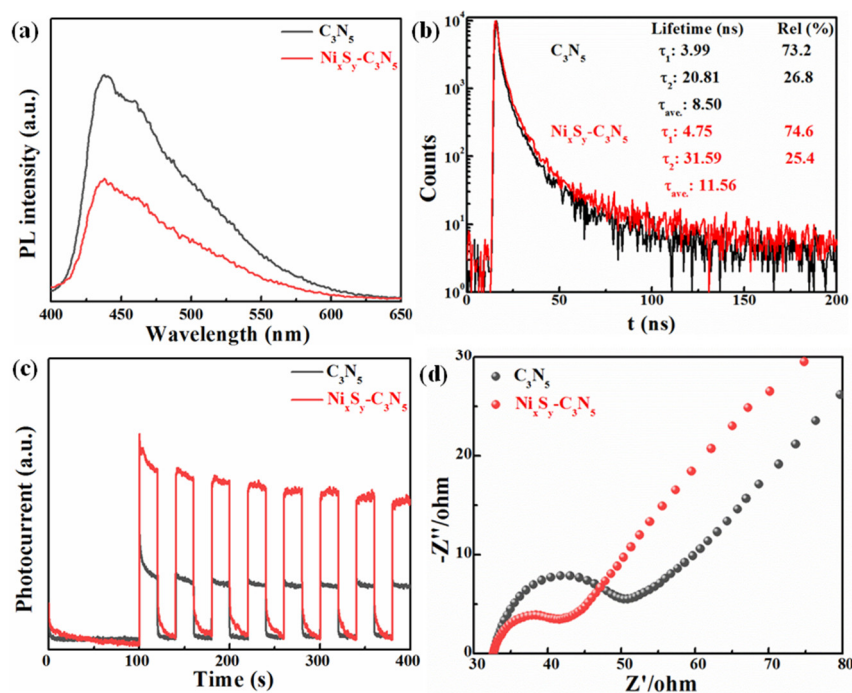


Figure 10. Comparison of steady-state (a) and time-resolved (b) fluorescence spectra as well as photocurrent-time (c) and EIS (d) behaviors of C_3N_5 and $\text{Ni}_x\text{S}_y\text{-C}_3\text{N}_5$.

Based on the above results, the mechanism for photocatalytic H_2 production or NO oxidation is proposed. Under visible light irradiation, C_3N_5 is excited and generates e^-/h^+ pairs. Ni_xS_y can harvest the e^- on the CB of C_3N_5 , and then the trapped electrons participate in subsequent surface reactions. For H_2 production, the collected electrons on Ni_xS_y react with adsorbed H_2O molecules and H_2 is produced. The residual h^+ on the VB of C_3N_5 is consumed by TEOA, and subsequently the whole photocatalytic H_2 production procedure is accomplished. In the process of photocatalytic NO oxidation, the activation of O_2 is considered the first step according to most reported studies. The generation of ROS such as $\bullet\text{O}_2^-$, $^1\text{O}_2$ and $\bullet\text{OH}$ are enhanced by Ni_xS_y , as discussed in the above section. These ROS and the residual h^+ on the VB of C_3N_5 can then participate in the NO oxidation procedure along with the formation of NO_3^- and NO_2 .

3. Materials and Methods

3.1. Material Preparation

All chemicals used were purchased commercially and used without purification. C_3N_5 was prepared by heating 3-amino-1,2,4-triazole under 500°C in air according to our previous work [27]. Generally, $\text{Ni}_x\text{S}_y\text{-C}_3\text{N}_5$ was synthesized by the hydrothermal method at 120°C . In brief, C_3N_5 was dispersed in 40 mL deionized water, followed by the addition of $\text{Ni}(\text{NO}_3)_2$ and thioacetamide (TAA) with a mol ratio of 1:3, and then transferred into a 100 mL Teflon-lined autoclave. Finally, the autoclave was sealed and kept at 120°C for 12 h. The precipitate was washed with distilled water and absolute ethanol several times after the autoclave cooled to room temperature. The obtained samples were dried in vacuum at 80°C for 12 h. The loading amount of Ni_xS_y on C_3N_5 was calculated based on

the initial input Ni ion mass fraction, and a series of $\text{Ni}_x\text{S}_y\text{-C}_3\text{N}_5$ hybrids with an Ni_xS_y loading amount varying between 0.5 and 4.0 wt% were prepared by changing the amount of $\text{Ni}(\text{NO}_3)_2$ and TAA accordingly. Pristine Ni_xS_y was also prepared by the same method in the absence of C_3N_5 . Notably, all the materials containing Ni_xS_y in the following section were prepared under 120 °C hydrothermal conditions unless otherwise specified.

3.2. Catalyst Characterization

XRD patterns were recorded on a powder X-ray diffractometer with Cu K α radiation (D8 Advance Bruker Inc., Munich, Germany). TEM and HRTEM images were acquired using FEI TALOS F200. SEM and EDS mapping images were acquired using Gemini Sigma 300. The Brunauer–Emmett–Teller (BET) specific surface area was evaluated using a nitrogen adsorption–desorption apparatus (ASAP 2040, Micrometrics Inc., Norcross, GA, USA), with all samples degassed at 120 °C for 12 h prior to measurements. The valence state of each element in the catalyst was analyzed by X-ray photoelectron spectroscopy (XPS) on a Thermo Fisher ESCALAB 250Xi X-ray photoelectron spectroscope. A Shimadzu UV-3100 recording spectrophotometer and fluorescence spectrometer (F-4600, Hitachi Inc., Tokyo, Japan) were used to record UV-vis diffuse reflectance (DRS) and PL spectra measurements, respectively. Time-resolved fluorescence spectra (TRFS) were obtained on an Edinburgh FLS 1000. Electron paramagnetic resonance (EPR) spectra were recorded on a JES-FA200 EPR Spectrometer. DMPO (5,5-dimethyl-1-pyrroline-*N*-oxide) was used as radical spin-trapped reagent for $\bullet\text{OH}$ and $\bullet\text{O}_2^-$. TEMP (2,2,6,6-tetramethylpiperidine) was used as the trapping agent for $^1\text{O}_2$ [11].

The photocurrent and electrochemical impedance measurements were recorded on a CHI 660D electrochemical workstation (Chenhua Instrument, Shanghai, China) with a conventional three-electrode configuration. Pt foil and Ag/AgCl (saturated KCl) were used as the counter electrode and reference electrode, respectively. The working electrode was made by spreading catalyst/naion slurry on FTO glass and 0.1 M Na_2SO_4 aqueous solution was used as the electrolyte.

3.3. Photocatalytic Activity Tests

The photocatalytic H_2 production rate and AQY measurements were carried out on a top-irradiated reaction vessel containing catalyst and sacrificial reagent (TEOA) connected to a closed gas system with a 300 W Xe-lamp (PLS SXE300, Beijing Perfectlight Inc., China) equipped with a cutoff filter ($\lambda > 420$ nm) or band-pass filters ($\lambda = 420, 500$ nm etc.); the operation system is shown in Figure S5. The H_2 production rate was detected by a GC (SP7820, TCD detector, 5 Å molecular sieve columns, and Ar carrier), and AQY values were calculated according to our previous report [27]:

$$\text{AQY} = 2 \times (\text{Number of evolved } \text{H}_2 \text{ molecules}) / (\text{Number of incident photons})$$

For photocatalytic NO removal, a continuous flow reactor under ambient conditions was adopted, as per our previous work [11]. The volume of the rectangular reactor was 4.5 L (30 cm \times 15 cm \times 10 cm). A 25 mg catalyst was dispersed into the mixture of ethanol and water and then transferred into a culture dish with a diameter of 12 cm, and the dish was then placed in the reactor after the solvent was evaporated. A 30 W visible LED (General Electric) was used as a light source. The gas (containing NO and air) flow rate through the reactor was controlled at 1000 mL/min by a mass flow controller with an initial NO concentration of ~ 600 ppb. The NO and NO_2 concentrations were recorded on a NO_x analyzer model T200 (Teledyne API). The generation of NO_3^- was detected by ion chromatography on Thermo DIONEX ICS-900.

4. Conclusions

In summary, a low-cost and noble-metal-free 2D $\text{Ni}_x\text{S}_y\text{-C}_3\text{N}_5$ hybrid photocatalyst was facially fabricated by a hydrothermal procedure under a low temperature and analyzed using a series of methods. The tight contact between 2D Ni_xS_y and 2D C_3N_5 sheets facilitates

internal photogenerated electron transfer from C_3N_5 to Ni_xS_y , which is demonstrated by steady-state and time-resolved PL spectra as well as light-switched photocurrent behavior. The $Ni_xS_y-C_3N_5$ hybrid possesses multiple photocatalytic applications (H_2 production from water and NO removal) with high activity and stability. In particular, the optimal $Ni_xS_y-C_3N_5$ photocatalyst exhibits a high AQY value of 37.0% at 420 nm, exceeding Pt- C_3N_5 material and revealing the potential of the Ni_xS_y in photocatalytic water splitting. This work not only demonstrates a simple method with which to construct a high-efficiency noble-metal-free hybrid photocatalyst, but it also exhibits the potential applications of such a photocatalyst in various fields.

Supplementary Materials: The following are available online at <https://www.mdpi.com/article/10.3390/catal11091089/s1>, Figure S1, XRD patterns of Ni_xS_y prepared under different hydrothermal temperatures; Figure S2, XPS survey spectrum of $Ni_xS_y-C_3N_5$ (a) and high-resolution spectra of C 1s (b) and N 1s (c); Figure S3, Influence of mole ratio of Ni/S on the H_2 production activity of 3.0 wt% $Ni_xS_y-C_3N_5$; Figure S4, Comparison of nitrogen adsorption–desorption isotherms between C_3N_5 and $Ni_xS_y-C_3N_5$; Figure S5, Photograph of photocatalytic H_2 production system.

Author Contributions: Conceptualization, X.Z. and Y.Y.; methodology, C.P., J.H., L.S. and S.W.; formal analysis, L.H. and C.P.; investigation, L.H.; data curation, L.H. and C.P.; writing—original draft preparation, L.H.; writing—review and editing, X.Z. and Y.Y.; supervision, X.Z. and Y.Y.; project administration, X.Z.; funding acquisition, X.Z. and Y.Y. All authors have read and agreed to the published version of the manuscript.

Funding: This work was financially supported by the National Natural Science Foundation of China (21703075, 51872107, 52073110, and 22002047), Natural Science Foundation of Hubei Province (2020CFB694) and Fundamental Research Funds for the Central Universities (2662020LXPY005).

Data Availability Statement: All the data presented in this article are available at <https://doi.org/10.6084/m9.figshare.16586414> (accessed on 8 September 2021).

Conflicts of Interest: The authors declare no conflict of interest.

References

1. Yang, H.; He, C.; Fu, L.; Huo, J.; Zhao, C.; Li, X.; Song, Y. Capture and separation of CO_2 on BC_3 nanosheets: A DFT study. *Chin. Chem. Lett.* **2021**. [CrossRef]
2. Fu, L.; Wang, R.; Zhao, C.; Huo, J.; He, C.; Kim, K.; Zhang, W. Construction of Cr-embedded graphyne electrocatalyst for highly selective reduction of CO_2 to CH_4 : A DFT study. *Chem. Eng. J.* **2021**, *414*, 128857. [CrossRef]
3. Wang, R.; He, C.; Chen, W.; Zhao, C.; Huo, J. Rich B active centers in Penta- B_2C as high-performance photocatalyst for nitrogen reduction. *Chin. Chem. Lett.* **2021**. [CrossRef]
4. Shen, R.; Ding, Y.; Li, S.; Zhang, P.; Xiang, Q.; Ng, Y.; Li, X. Constructing low-cost Ni_3C /twin-crystal $Zn_{0.5}Cd_{0.5}S$ heterojunction/homojunction nanohybrids for efficient photocatalytic H_2 evolution. *Chin. J. Catal.* **2021**, *42*, 25–36. [CrossRef]
5. Wageh, S.; Al-Ghamdi, A.; Jafer, R.; Li, X.; Zhang, P. A new heterojunction in photocatalysis: S-scheme heterojunction. *Chin. J. Catal.* **2021**, *42*, 667–669. [CrossRef]
6. Wang, J.; Kuo, M.; Zeng, P.; Xu, L.; Chen, S.; Peng, T. Few-layer $BiVO_4$ nanosheets decorated with $SrTiO_3$: Rh nanoparticles for highly efficient visible-light-driven overall water splitting. *Appl. Catal. B Environ.* **2020**, *279*, 119377. [CrossRef]
7. Jiang, Z.; Chen, Q.; Zheng, Q.; Shen, R.; Zhang, P.; Li, X. Constructing 1D/2D Schottky-Based Heterojunctions between $Mn_{0.2}Cd_{0.8}S$ Nanorods and Ti_3C_2 Nanosheets for Boosted Photocatalytic H_2 Evolution. *Acta Phys. Chim. Sin.* **2021**, *37*, 2010059.
8. Shen, R.; Ren, D.; Ding, Y.; Guan, Y.; Ng, Y.; Zhang, P.; Li, X. Nanostructured CdS for efficient photocatalytic H_2 evolution: A review. *Sci. China Mater.* **2020**, *63*, 2153–2188. [CrossRef]
9. Sun, W.; Xiang, Y.; Jiang, Z.; Wang, S.; Yang, N.; Jin, S.; Sun, L.; Teng, H.; Chen, H. Designed polymeric conjugation motivates tunable activation of molecular oxygen in heterogeneous organic photosynthesis. *Sci. Bull.* **2021**. [CrossRef]
10. Zhang, X.; Han, L.; Chen, H.; Wang, S. Direct catalytic nitrogen oxide removal using thermal, electrical or solar energy. *Chin. Chem. Lett.* **2021**. [CrossRef]
11. Wang, S.; Ding, X.; Zhang, X.; Pang, H.; Hai, X.; Zhan, G.; Zhou, W.; Song, H.; Zhang, L.; Chen, H.; et al. In Situ Carbon Homogeneous Doping on Ultrathin Bismuth Molybdate: A Dual-Purpose Strategy for Efficient Molecular Oxygen Activation. *Adv. Funct. Mater.* **2017**, *27*, 1703923. [CrossRef]
12. Xu, Q.; Zhang, L.; Cheng, B.; Fan, J.; Yu, J. S-Scheme Heterojunction Photocatalyst. *Chem* **2020**, *6*, 1543–1559. [CrossRef]
13. Xu, F.; Meng, K.; Cheng, B.; Wang, S.; Xu, J.; Yu, J. Unique S-scheme heterojunctions in self-assembled $TiO_2/CsPbBr_3$ hybrids for CO_2 photoreduction. *Nat. Commun.* **2020**, *11*, 4613. [CrossRef]

14. Wang, X.; Maeda, K.; Thomas, A.; Takanabe, K.; Xin, G.; Carlsson, J.; Domen, K.; Antonietti, M. A metal-free polymeric photocatalyst for hydrogen production from water under visible light. *Nat. Mater.* **2009**, *8*, 76–80. [[CrossRef](#)] [[PubMed](#)]
15. Xia, P.; Antonietti, M.; Zhu, B.; Heil, T.; Yu, J.; Cao, S. Designing Defective Crystalline Carbon Nitride to Enable Selective CO₂ Photoreduction in the Gas Phase. *Adv. Funct. Mater.* **2019**, *29*, 1900093. [[CrossRef](#)]
16. Lin, L.; Lin, Z.; Zhang, J.; Cai, X.; Lin, W.; Yu, Z.; Wang, X. Molecular-level insights on the reactive facet of carbon nitride single crystals photocatalysing overall water splitting. *Nat. Catal.* **2020**, *3*, 649–655. [[CrossRef](#)]
17. Fu, J.; Xu, Q.; Low, J.; Jiang, C.; Yu, J. Ultrathin 2D/2D WO₃/g-C₃N₄ step-scheme H₂-production photocatalyst. *Appl. Catal. B Environ.* **2019**, *243*, 556–565. [[CrossRef](#)]
18. Zhao, D.; Dong, C.; Wang, B.; Chen, C.; Huang, Y.; Diao, Z.; Li, S.; Guo, L.; Shen, S. Synergy of dopants and defects in graphitic carbon nitride with exceptionally modulated band structures for efficient photocatalytic oxygen evolution. *Adv. Mater.* **2019**, *31*, 1903545. [[CrossRef](#)]
19. Zhao, D.; Wang, Y.; Dong, C.; Huang, Y.; Chen, J.; Xue, F.; Shen, S.; Guo, L. Boron-doped nitrogen-deficient carbon nitride-based Z-scheme heterostructures for photocatalytic overall water splitting. *Nat. Energy* **2021**, *6*, 388–397. [[CrossRef](#)]
20. Liu, D.; Chen, D.; Li, N.; Xu, Q.; Li, H.; He, J.; Lu, J. Surface Engineering of g-C₃N₄ by Stacked BiOBr Sheets Rich in Oxygen Vacancies for Boosting Photocatalytic Performance. *Angew. Chem. Int. Ed.* **2020**, *59*, 4519–4524. [[CrossRef](#)]
21. Zhang, J.; Jing, B.; Tang, Z.; Ao, Z.; Xia, D.; Zhu, M.; Wang, S. Experimental and DFT insights into the visible-light driving metal-free C₃N₅ activated persulfate system for efficient water purification. *Appl. Catal. B Environ.* **2021**, *289*, 120023. [[CrossRef](#)]
22. Kumar, P.; Vahidzadeh, E.; Thakur, U.; Kar, P.; Alam, K.; Goswami, A.; Mahdi, N.; Cui, K.; Bernard, G.; Michaelis, V.; et al. C₃N₅: A Low Bandgap Semiconductor Containing an Azo-Linked Carbon Nitride Framework for Photocatalytic, Photovoltaic and Adsorbent Applications. *J. Am. Chem. Soc.* **2019**, *141*, 5415–5436. [[CrossRef](#)] [[PubMed](#)]
23. Li, M.; Lu, Q.; Liu, M.; Yin, P.; Wu, C.; Li, H.; Zhang, Y.; Yao, S. Photoinduced Charge Separation via the Double-Electron Transfer Mechanism in Nitrogen Vacancies g-C₃N₅/BiOBr for the Photoelectrochemical Nitrogen Reduction. *ACS Appl. Mater. Interfaces* **2020**, *12*, 38266–38274. [[CrossRef](#)] [[PubMed](#)]
24. Kim, I.Y.; Kim, S.; Jin, X.; Premkumar, S.; Chandra, G.; Lee, N.S.; Mane, G.P.; Hwang, S.J.; Umopathy, S.; Vinu, A. Ordered mesoporous C₃N₅ with a combined triazole and triazine framework and its graphene hybrids for the oxygen reduction reaction (ORR). *Angew. Chem. Int. Ed.* **2018**, *57*, 17381–17386. [[CrossRef](#)]
25. Mane, G.P.; Talapaneni, S.N.; Lakhi, K.S.; Ilbeygi, H.; Ravon, U.; Al-Bahily, K.; Mori, T.; Park, D.H.; Vinu, A. Highly ordered nitrogen-rich mesoporous carbon nitrides and their superior performance for sensing and photocatalytic hydrogen generation. *Angew. Chem. Int. Ed.* **2017**, *56*, 8481–8485. [[CrossRef](#)] [[PubMed](#)]
26. Liu, T.; Yang, G.; Wang, W.; Wang, C.; Wang, M.; Sun, X.; Xu, P.; Zhang, J. Preparation of C₃N₅ nanosheets with enhanced performance in photocatalytic methylene blue (MB) degradation and H₂-evolution from water splitting. *Environ. Res.* **2020**, *188*, 109741. [[CrossRef](#)]
27. Peng, C.; Han, L.; Huang, J.; Wang, S.; Zhang, X.; Chen, H. Comprehensive investigation on robust photocatalytic hydrogen production over C₃N₅. *Chin. J. Catal.* **2021**. [[CrossRef](#)]
28. Wang, H.; Zhang, W.; Zhang, X.; Hu, S.; Zhang, Z.; Zhou, W.; Liu, H. Multi-interface collaboration of graphene cross-linked NiS-NiS₂-Ni₃S₄ polymorph foam towards robust hydrogen evolution in alkaline electrolyte. *Nano Res.* **2021**. [[CrossRef](#)]
29. Vijaya, S.; Landi, G.; Wu, J.J.; Anandan, S. Ni₃S₄/CoS₂ mixed-phase nanocomposite as counter electrode for Pt-free dye-sensitized solar cells. *J. Power Sources* **2020**, *478*, 229068. [[CrossRef](#)]
30. Zou, H.; He, B.; Kuang, P.; Yu, J.; Fan, K. Ni_xS_y nanowalls/nitrogen-doped graphene foam is an efficient trifunctional catalyst for unassisted artificial photosynthesis. *Adv. Funct. Mater.* **2018**, *28*, 1706917. [[CrossRef](#)]
31. Yu, L.; Wu, L.; McElhenny, B.; Song, S.; Luo, D.; Zhang, F.; Yu, Y.; Chen, S.; Ren, Z. Ultrafast room-temperature synthesis of porous S-doped Ni/Fe (oxy) hydroxide electrodes for oxygen evolution catalysis in seawater splitting. *Energy Environ. Sci.* **2020**, *13*, 3439–3446. [[CrossRef](#)]
32. Zhang, G.; Feng, Y.S.; Lu, W.T.; He, D.; Wang, C.Y.; Li, Y.K.; Wang, X.Y.; Cao, F.F. Enhanced catalysis of electrochemical overall water splitting in alkaline media by Fe doping in Ni₃S₂ nanosheet arrays. *ACS Catal.* **2018**, *8*, 5431–5441. [[CrossRef](#)]
33. Yan, A.; Shi, X.; Huang, F.; Fujitsuka, M.; Majima, T. Efficient photocatalytic H₂ evolution using NiS/ZnIn₂S₄ heterostructures with enhanced charge separation and interfacial charge transfer. *Appl. Catal. B Environ.* **2019**, *250*, 163–170. [[CrossRef](#)]
34. Wang, B.; Ding, Y.; Deng, Z.; Li, Z. Rational design of ternary NiS/CQDs/ZnIn₂S₄ nanocomposites as efficient noble-metal-free photocatalyst for hydrogen evolution under visible light. *Chin. J. Catal.* **2019**, *40*, 335–342. [[CrossRef](#)]
35. Zhao, X.; Feng, J.; Liu, J.; Shi, W.; Yang, G.; Wang, G.C.; Cheng, P. An Efficient, Visible-Light-Driven, Hydrogen Evolution Catalyst NiS/Zn_xCd_{1-x}S Nanocrystal Derived from a Metal-Organic Framework. *Angew. Chem. Int. Ed.* **2018**, *130*, 9938–9942. [[CrossRef](#)]
36. Wen, J.; Li, X.; Li, H.; Ma, S.; He, K.; Xu, Y.; Fang, Y.; Liu, W.; Gao, Q. Enhanced visible-light H₂ evolution of g-C₃N₄ photocatalysts via the synergetic effect of amorphous NiS and cheap metal-free carbon black nanoparticles as co-catalysts. *Appl. Surf. Sci.* **2015**, *358*, 204–212. [[CrossRef](#)]
37. Zhao, H.; Zhang, H.; Cui, G.; Dong, Y.; Wang, G.; Jiang, P.; Wu, X.; Zhao, N. A photochemical synthesis route to typical transition metal sulfides as highly efficient cocatalyst for hydrogen evolution: From the case of NiS/g-C₃N₄. *Appl. Catal. B Environ.* **2018**, *225*, 284–290. [[CrossRef](#)]

38. Wang, S.; Ding, X.; Yang, N.; Zhan, G.; Zhang, X.; Dong, G.; Zhang, L.; Chen, H. Insight into the effect of bromine on facet-dependent surface oxygen vacancies construction and stabilization of Bi₂MoO₆ for efficient photocatalytic NO removal. *Appl. Catal. B Environ.* **2020**, *265*, 118585. [[CrossRef](#)]
39. Zhang, R.; Zhang, A.; Cao, Y.; Wang, S.; Dong, F.; Zhou, Y. Mo-doped carbon nitride homojunction to promote oxygen activation for enhanced photocatalytic performance. *Chem. Eng. J.* **2020**, *401*, 126028. [[CrossRef](#)]
40. Cao, Y.; Zhang, R.; Zheng, Q.; Cui, W.; Liu, Y.; Zheng, K.; Dong, F.; Zhou, Y. Dual functions of O-atoms in the g-C₃N₄/BO_{0.2}N_{0.8} interface: Oriented charge flow in-plane and separation within the interface to collectively promote photocatalytic molecular oxygen activation. *ACS Appl. Mater. Interfaces* **2020**, *12*, 34432–34440. [[CrossRef](#)] [[PubMed](#)]
41. Wang, Z.; Huang, Y.; Chen, M.; Shi, X.; Zhang, Y.; Cao, J.; Ho, W.; Lee, S.C. Roles of N-vacancies over porous g-C₃N₄ microtubes during photocatalytic NO_x removal. *ACS Appl. Mater. Interfaces* **2019**, *11*, 10651–10662. [[CrossRef](#)]
42. Yang, X.; Wang, S.; Chen, T.; Yang, N.; Jiang, K.; Wang, P.; Li, S.; Ding, X.; Chen, H. Chloridion-induced dual tunable fabrication of oxygen-deficient Bi₂WO₆ atomic layers for deep oxidation of NO. *Chin. J. Catal.* **2021**, *42*, 1013–1023. [[CrossRef](#)]
43. Kou, M.; Deng, Y.; Zhang, R.; Wang, L.; Wong, P.K.; Su, F.; Ye, L. Molecular oxygen activation enhancement by BiOBr_{0.5}I_{0.5}/BiOI utilizing the synergistic effect of solid solution and heterojunctions for photocatalytic NO removal. *Chin. J. Catal.* **2020**, *41*, 1480–1487. [[CrossRef](#)]
44. Shi, X.; Wang, P.; Li, W.; Bai, Y.; Xie, H.; Zhou, Y.; Ye, L. Change in photocatalytic NO removal mechanisms of ultrathin BiOBr/BiOI via NO₃-adsorption. *Appl. Catal. B Environ.* **2019**, *243*, 322–329. [[CrossRef](#)]
45. Zhang, X.; Xiao, J.; Hou, M.; Xiang, Y.; Chen, H. Robust visible/near-infrared light driven hydrogen generation over Z-scheme conjugated polymer/CdS hybrid. *Appl. Catal. B Environ.* **2018**, *224*, 871–876. [[CrossRef](#)]
46. Zhang, X.; Peng, T.; Yu, L.; Li, R.; Li, Q.; Li, Z. Visible/near-infrared-light-induced H₂ production over g-C₃N₄ co-sensitized by organic dye and zinc phthalocyanine derivative. *ACS Catal.* **2015**, *5*, 504–510. [[CrossRef](#)]
47. Wang, J.; Wang, G.; Cheng, B.; Yu, J.; Fan, J. Sulfur-doped g-C₃N₄/TiO₂ S-scheme heterojunction photocatalyst for Congo Red photodegradation. *Chin. J. Catal.* **2021**, *42*, 56–68. [[CrossRef](#)]